ChemComm

Local Density Changes and Carbonate Rotation Enable Ba Incorporation in Amorphous Calcium Carbonate

Journal:	*ChemComm*
Manuscript ID	CC-COM-02-2023-000959.R2
Article Type:	Communication

COMMUNICATION

Local Density Changes and Carbonate Rotation Enable Ba Incorporation in Amorphous Calcium Carbonate

Sebastien N. Kerisit,*[a] Micah P. Prange,[a] and Sebastian T. Mergelsberg[a]

Received 00th January 20xx,
Accepted 00th January 20xx

DOI: 10.1039/x0xx00000x

Incorporation of a Ba impurity in amorphous calcium carbonate (ACC) is shown with ab initio molecular dynamics simulation to have a long-range effect on its atomic-level structure and to be energetically favoured relative to incorporation in crystalline calcium carbonate polymorphs. The ability of carbonate ions to rotate and of ACC to undergo local density changes explain ACC's propensity for incorporating divalent metal impurities with a wide range of ionic radii. These findings provide an atomic-level basis for understanding the significant effects of low concentrations of impurities on the structure of ACC.

The incorporation of minor or trace elements—referred to generally as impurities here—in minerals during growth has significant implications for a broad spectrum of research topics including the fate and transport of contaminants, bio-availability of nutrients, bio-mineralization, and paleo-climate reconstruction. Impurity incorporation in carbonate minerals is particularly salient to these fields of research due to their ubiquity in both geological and biological systems. Moreover, carbonate minerals such as calcite ($CaCO_3$) are known to accommodate a wide range of impurities (divalent cations, rare-earth elements, actinides, oxyanions, etc.). For example, many of the divalent cations that form common carbonate phases are also contaminants and include Pb, ^{90}Sr, Cd, ^{60}Co, and Ni ($PbCO_3$ and $SrCO_3$ adopt the aragonite ($CaCO_3$) crystal structure, in which the cation is in nine-fold coordination, whereas $CdCO_3$, $CoCO_3$, and $NiCO_3$ adopt the calcite structure, in which the cation is in six-fold coordination). These divalent cations span a large range of ionic radii. Pb^{2+} ($r_{9\text{-fold}}$=1.35 Å) and Sr^{2+} ($r_{9\text{-fold}}$=1.31 Å) are larger than Ca^{2+} ($r_{9\text{-fold}}$=1.18 Å, $r_{6\text{-fold}}$=1.00 Å) whereas Cd^{2+} ($r_{6\text{-fold}}$=0.95 Å) is closest in size to Ca^{2+}, and Co^{2+} ($r_{6\text{-fold}}$=0.745 Å) and Ni^{2+} ($r_{6\text{-fold}}$=0.69 Å) are much smaller.[2] Crystallization pathways are expected to influence the extent of divalent metal cation incorporation in carbonate minerals. For example, Littlewood et al.[3] reported that homogeneous calcite formation through an amorphous calcium carbonate (ACC) intermediate could enhance Sr incorporation in calcite relative to direct calcite formation. Sr is known to have limited solubility in calcite because of its larger ionic radius. Therefore, we hypothesize that the enhancement in impurity incorporation in calcite afforded by an ACC intermediate is greater the larger the difference in ionic radius between the divalent cation and Ca^{2+} is. We are pursuing a combined experimental–computational research campaign that considers a wide range of divalent metal cation impurities to address this hypothesis. In this communication, we report the first computational results of this campaign obtained for Ba incorporation in ACC. Ba^{2+} is of significant interest because it is the largest divalent cation ($r_{9\text{-fold}}$=1.47 Å) to form the aragonite structure and is thus expected to show the largest effect. For example, amorphous calcium barium carbonate, $Ca_{1-x}Ba_xCO_3{\cdot}nH_2O$, has been synthesized with a Ba content up to x=0.55,[1] whereas the solubility of Ba in calcite and aragonite is approximately 1%.[4, 5] Moreover, although there is evidence that amorphous barium carbonate (ABC) is a transient intermediate phase during witherite ($BaCO_3$) crystallization,[6, 7] its short lifetime has prevented its characterization by total scattering measurements,[8] and atomistic computer simulations are thus a valuable tool to gain insight into its short-range structure. Our atomistic simulations shed light on the coordination environment of Ba in ACC, the structural changes ACC undergoes to accommodate an isolated Ba impurity, and the energetics of Ba incorporation in ACC relative to that in crystalline calcium carbonate polymorphs.

We performed ab initio molecular dynamics (AIMD) simulations based on density functional theory (see ESI for details). The protocol used to generate amorphous structural models was that described by Prange et al.[9] Briefly, randomly generated structures of $Ba_xCa_{1-x}CO_3{\cdot}H_2O$, where x = 0 (ACC), 0.04167 (ACC(Ba)), or 1 (ABC), were first relaxed with classical molecular dynamics at 300 K and then subjected to an AIMD melt-quench procedure whereby the initial structures were melted at 1500 K and quenched to 300 K at a rate of 300 K ps^{-1}.

[a] Physical and Computational Sciences Directorate, Pacific Northwest National Laboratory, Richland, Washington 99352, United States.
Electronic Supplementary Information (ESI) available: [details of any supplementary information available should be included here]. See DOI: 10.1039/x0xx00000x

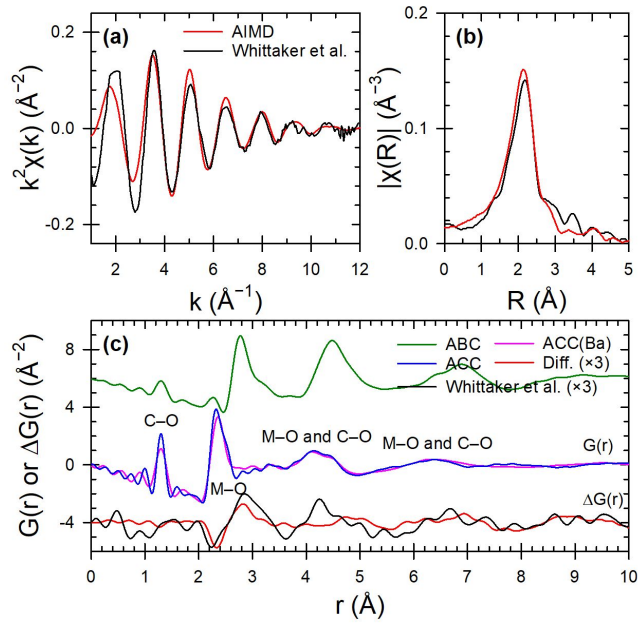

Fig. 2 (a) Calculated and measured Ba K-edge EXAFS spectrum (ΔE_0 = −1 eV) and (b) corresponding Fourier transform magnitudes (3 Å^{-1} ≤ k ≤ 12 Å^{-1}, weighted by k^2, Hanning window with dk = 1 Å^{-1}). The experimental spectrum is from Whittaker et al.[1] and was scaled to match the intensity of the peak at approximately 8 Å^{-1} because the k^{2}χ(k) magnitudes were not available. (c) X-ray PDF, G(r), simulated using AIMD ensembles generated for ABC, ACC, and ACC(Ba) and calculated and measured ACC(Ba)–ACC differential PDFs, ΔG(r), (Q_{max} = 17 Å^{-1}). The normalized scattering data [I(Q)] used to generate the measured ΔG(r) is from Whittaker et al.[1]

The quenched configurations were then run with AIMD in the NVT ensemble for 12 ps, followed by 12 ps in the NPT ensemble. For ACC and ABC, six configurations were pulled from the melt at 9-ps intervals, with the first configuration pulled at 16 ps. For ACC(Ba), 30 configurations were pulled from the melt at 6-ps intervals, with the first configuration pulled at 7 ps.

The AIMD trajectories of ACC(Ba) were used to compute the Ba K-edge EXAFS (extended X-ray absorption fine structure spectroscopy) spectrum (Fig. 2), using the approach described in Prange et al.[9] and references therein, and compare it to the experimental spectrum reported by Whittaker et al.[1] from room temperature measurements with a similar $BaCO_3$ mole fraction (0.05). The hydration level used here (n=1) was consistent with that in Whittaker et al. (n=1.2±0.2). The agreement was good, showing that the AIMD simulations accurately described the coordination environment of a Ba impurity in ACC.

X-ray pair distribution functions (PDF) were also computed from the AIMD trajectories of ABC, ACC, and ACC(Ba) (Fig. 2). The peak corresponding to the nearest-neighbour M–O distances was pushed to longer distances in ABC relative to ACC due to the much larger ionic radius of Ba^{2+} compared to that of Ca^{2+}. A small peak remained at approximately 2.3 Å due to intramolecular carbonate O–O distances. The difference between the G(r) profiles of ACC(Ba) and ACC showed a depression where Ca–O distances were located and a bump on the high-r side of the M–O peak in good agreement with the measured differential PDF. Small but discernible differences also appeared at higher r—beyond half the mean distance between Ba impurities (≈6.4 Å)—as valley-peak oscillatory features, indicating that the mismatch in cation ionic radius was the primary cause of the differential features. This analysis showed that the effect of a Ba impurity on the atomic-level structure of ACC was long ranged and should be detectable even for mole fractions as low as 0.05 by careful analysis of the X-ray PDF.

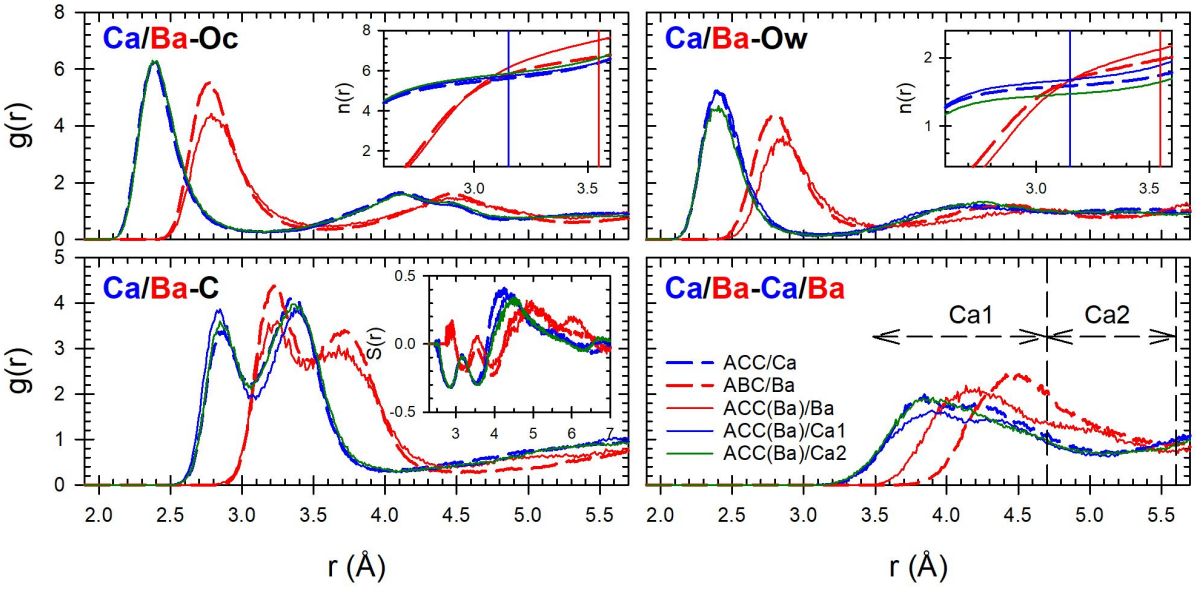

Fig. 1. Radial distribution functions (g(r)) of Ca and Ba with carbonate oxygen (Oc), water oxygen (Ow), carbon (C), and each other in ABC, ACC, and ACC(Ba). The upper insets show the number of atoms as a function of distance (n(r)) with the positions of the first g(r) minima shown as vertical lines. The lower inset shows the orientation order parameter of the angle between the Ca/Ba–C vector and the normal to the carbonate plane as a function of the Ca/Ba–C distance (S(r)).

The concentration of Ba in ACC(Ba) was 24 times lower than that of Ba in ABC and Ca in ACC, thus a much larger number of configurations were generated (30). Figures S1 and S2 (ESI) showed that 30 configurations were sufficient to converge the Ba–O, Ba–C, and Ba–Ca radial distribution functions (RDF). For both carbonate oxygen (Oc) and water oxygen (Ow) ligands, the Ba–O RDFs showed a diminished magnitude of the first maximum in ACC(Ba) relative to ABC (**Error! Reference source not found.**), which was accompanied by a shift of the first peak position to longer distances (from 2.76 Å to 2.79 Å for Ba–Oc and from 2.79 Å to 2.85 Å for Ba–Ow). The mean Ba–Oc and Ba–Ow distances, obtained from fitting the g(r) up to 3.2 Å with a skewed normal distribution,[10] increased from 2.84 Å to 2.89 Å and from 2.86 Å to 2.93 Å, respectively. Therefore, Ba coordination was disrupted in ACC relative to that in ABC. However, the tail of the first peak showed an increased magnitude, which translated to a significant increase of the Ba coordination number—defined as the value of n(r) at the first minimum of g(r) (upper insets of **Error! Reference source not found.**)—for Ba in ACC (9.63) relative to Ba in ABC (8.67) (**Error! Reference source not found.**). The distribution of instantaneous CNs of Ba in ACC retained the same shape as that of Ba in ABC but was shifted towards higher values by 1 (**Error! Reference source not found.**). In contrast, the relative proportions of monodentate carbonate oxygen, bidentate carbonate oxygen, and water oxygen ligands were not significantly affected (**Error! Reference source not found.**). The partition into the three types of ligands was thus controlled by the ionic radius of the divalent cation. The orientation order parameter, defined as $S(r) = \left\langle \left(\sum_{i=1}^{N_C} 0.5 \times \left(3\cos^2 \theta_i - 1\right) \right) / N_C \right\rangle$ where N_C is the number of carbonate ions and θ is the angle between the Ca/Ba–C vector and the normal to the carbonate plane defined by its three O atoms, showed that carbonate ligands of Ba in ABC adopted mostly an edge-on orientation (lower inset of Fig. 1; S equals −0.5, 1, and 0 for edge-on, face-on, and random orientations, respectively). The orientation of carbonate ligands of Ba in ACC was similar to that of Ba in ABC albeit slightly more random for monodentate carbonate ions.

Table 1. Coordination of Ba and Ca in ABC, ACC, and ACC(Ba) with mono- and bi-dentate carbonate oxygen (Oc) and water oxygen (Ow) ligands from NPT AIMD simulations. Coordination numbers (CN) are also tabulated.

System	Oc (mono-)	Oc (bi-)	Ow	CN
ABC/Ba	0.338	0.434	0.228	8.67
ACC(Ba)/Ba	0.353	0.427	0.220	9.63
ACC(Ba)/Ca1	0.399	0.375	0.226	7.41
ACC(Ba)/Ca2	0.447	0.352	0.201	7.32
ACC(Ba)/Ca3	0.440	0.330	0.230	7.33
ACC/Ca	0.431	0.348	0.221	7.20

To investigate the effect of the Ba impurity in ACC on the short-range structure of ACC, Ca atoms in ACC(Ba) were divided into three groups: those under the first peak (Ca1), those under the second peak (Ca2), and those beyond the second peak (Ca3) of the Ba–Ca RDF (**Error! Reference source not found.**). Figures S4 through S8 (ESI) showed that the Ca1/2/3–O, Ca1/2/3–C, and Ca1/2/3–Ca RDFs converged with 30 configurations. Ca atoms immediately surrounding the Ba impurity showed similar Ca–Oc

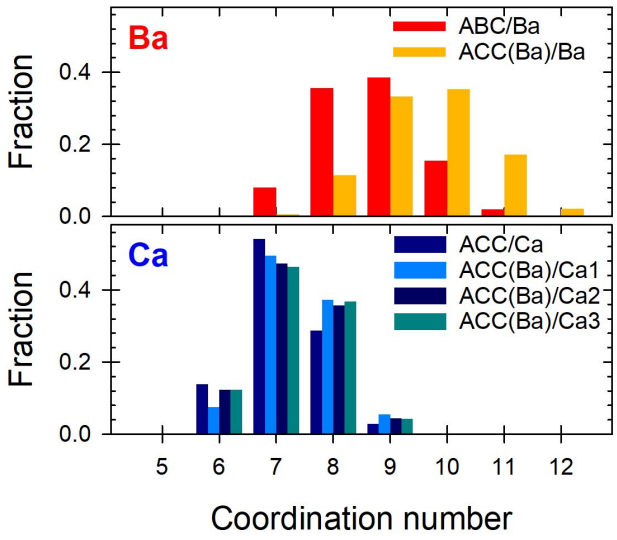

Fig. 3 Coordination numbers of Ba (top) and Ca (bottom) in ABC, ACC, and ACC(Ba).

and Ca–Ow RDFs than those in pure ACC, with only a slight increase of the magnitude of the tail of the first Ca–Ow peak (**Error! Reference source not found.**), which resulted in a small increase of the Ca CN in ACC(Ba) (7.41) relative to that in ACC (7.20) (**Error! Reference source not found.**). The conformation of the carbonate ligands was much more affected, as shown by an increase of the magnitude of the first Ca–C RDF peak (bidentate carbonate) with a corresponding decrease of the second Ca–C peak (monodentate carbonate), relative to those in ACC (**Error! Reference source not found.**). In contrast, the orientation of the carbonate ligands was little affected (lower inset of Fig. 1), indicating that the change in carbonate conformation resulted mainly from a rotation about the C_3 axis of symmetry of the carbonate. At the hydration level considered here (1 H_2O per MCO_3 unit), Ca and Ba had almost identical fractions of water ligands in their first coordination shells (0.22 for Ca in ACC and 0.23 for Ba in ABC; **Error! Reference source not found.**) indicating that this quantity was controlled by the H_2O/CO_3 ratio rather than by the ionic radii of the cations. However, the fractions of monodentate and bidentate carbonate oxygen ligands were opposite (0.43 and 0.35, respectively, for Ca in ACC and 0.34 and 0.43, respectively, for Ba in ACC; **Error! Reference source not found.**). Therefore, the larger Ba^{2+} cation caused the carbonate ligands in its first coordination shell to rotate, which forced an increase in coordination to bidentate carbonate ligands for Ca atoms immediately surrounding the Ba impurity (Ca1).

Ca atoms away from the Ba impurity (Ca3) had coordination environments that approximated that in ACC (the fractions of Oc(mono-) and Oc(bi-) were 0.440 and 0.330, respectively, compared to 0.431 and 0.348 in ACC) and a decreased CN relative to that of Ca1 that, however, did not reach that in ACC (**Error! Reference source not found.**). The CN distributions showed that this was due to a decrease of the fraction of Ca atoms with CN_{max} and an increase of the fraction of those with $CN_{max}+1$ (**Error! Reference source not found.**). Thus, even away from the Ba impurity, the amorphous material was predicted to be denser than pure ACC. An analysis of the molar volumes

supported this conclusion. The calculated molar volumes (with the standard error of the mean shown in parenthesis) of ACC and ABC were 51.48 (0.16) cm^3/mol and 63.23 (0.16) cm^3/mol, respectively. Based on those values, the predicted molar volume of an ideal solid solution with x=0.04167 would be 51.97 (0.15) cm^3/mol, which was higher than the calculated molar volume of 51.61 (0.10) cm^3/mol for ACC(Ba) (Table S1 of the ESI). Consistent with the higher CNs of both Ba and Ca relative to those in ABC and ACC, respectively (**Error! Reference source not found.**), ACC(Ba) was predicted to be denser than the corresponding solid solution.

The AIMD simulations also offered insights into the energetics of Ba incorporation in ACC relative to that in crystalline calcium carbonate phases. Figure S9 (ESI) showed that the internal energies of the 30 ACC(Ba) configurations approximated well a normal distribution. The mean internal energy of these configurations was used hereafter because Ba incorporation during ACC nucleation and growth was not expected to be an equilibrium process. NVT AIMD simulations (12 ps, preceded by a 1-ps equilibration period) of Ba in a 2×2×1 calcite or a 2×3×1 aragonite supercell (24 MCO_3 units) were performed, followed by a 12-ps NPT AIMD simulation. The same procedure was used for pure calcite and aragonite supercells. The energy of the reaction $Ba_xCa_{1-x}CO_3$(cr) + $CaCO_3{\cdot}H_2O$(am) → $CaCO_3$(cr) + $Ba_xCa_{1-x}CO_3{\cdot}H_2O$(am) with x=0.04167 was −0.29 eV and −0.21 eV (based on internal energies from NPT simulations) for calcite and aragonite, respectively. These energies of reaction pointed to the existence of a driving force for Ba to partition into ACC relative to calcite as well as relative to aragonite even though crystalline $BaCO_3$ adopts the aragonite structure. In other words, the structural flexibility of ACC translated to favourable energetics of impurity incorporation.

Carbonate rotation is a key source of structural flexibility. This phenomenon is not limited to amorphous carbonates. Carbonate rotation is one of the root causes of the disordered structure of vaterite ($CaCO_3$).[11] Carbonate ions can also rotate in calcite to accommodate divalent cation impurities at the calcium site.[12] But the lack of long-range order and the presence of water in amorphous carbonates magnify this effect. For example, carbonate rotation in amorphous intermediates facilitates the formation of crystalline phases that could not be formed directly. This is the case for balcite ($Ca_{0.5}Ba_{0.5}CO_3$), which forms through an amorphous intermediate and has a much higher Ba content than the Ba solubility limit in calcite.[13] This work shows that carbonate rotation also plays an important role in accommodating metal cation impurities in ACC. We speculate that rotation of the carbonate ion is facilitated by its lack of dipole moment. The long-range structural effect of impurities and the exothermic energetics of their incorporation in ACC may explain why low concentrations of additives have been shown to have significant impact on the short-range structure and kinetics of transformation of amorphous carbonates.[14]

In conclusion, when a Ba impurity is introduced in ACC, the size of its first coordination shell enlarges compared to that in ABC leading to a significant increase of the Ba CN. However, two aspects of ACC's structural flexibility enable it to accommodate the impurity. First, rotation of carbonate ligands allows the coordination environment of Ba in ACC to match the proportions of monodentate carbonate, bidentate carbonate, and water ligands in ABC. As a result, the larger Ba atom forces surrounding Ca atoms to increase their coordination to bidentate carbonate ligands. Second, while Ca atoms away from the Ba impurity recover the coordination environment of pure ACC, the Ca CN shows a small but distinct increase that reflects a densification of ACC in the presence of a Ba impurity, consistent with a non-ideal behaviour of the molar volume of ACC(Ba). Despite these long-ranged structural changes, Ba incorporation in ACC is energetically favoured relative to that in either calcite or aragonite. AIMD simulations of a range of divalent metal cations in ACC will determine to what extent the findings of this work vary with the ionic radius of the impurity.

Kerisit performed and analysed the AIMD simulations and wrote the original draft. Prange performed the X-ray PDF calculations. Mergelsberg processed the total scattering data. All authors reviewed and edited the manuscript.

This work was supported by the U.S. Department of Energy, Office of Science, Office of Basic Energy Sciences, Chemical Sciences, Geosciences, and Biosciences Division through its Geosciences program (FWP 56674) at Pacific Northwest National Laboratory (PNNL). PNNL is operated for DOE by the Battelle Memorial Institute under contract DE-AC05-76RL01830. The simulations were performed using PNNL Research Computing and the Environmental Molecular Sciences Laboratory (EMSL), a national scientific user facility sponsored by the U.S. DOE's Office of Biological and Environmental Research and located at PNNL in Richland, WA. The authors acknowledge Michael L. Whittaker and Derk Joester for providing total scattering data for ACC and Ba-containing ACC.

Conflicts of interest

There are no conflicts to declare.

References

1. M. L. Whittaker, W. Sun, K. A. DeRocher, S. Jayaraman, G. Ceder and D. Joester, *Adv. Funct. Mater.*, 2018, **28**, 1704202.
2. R. D. Shannon, *Act. Cryst. A*, 1976, **32**, 751-767.
3. J. L. Littlewood, S. Shaw, C. L. Peacock, P. Bots, D. Trivedi and I. T. Burke, *Cryst. Growth Des.*, 2017, **17**, 1214-1223.
4. A. J. Tesoriero and J. F. Pankow, *Geochim. Cosmochim. Acta*, 1996, **60**, 1053-1063.
5. M. Dietzel, N. Gussone and A. Eisenhauer, *Chem. Geol.*, 2004, **203**, 139-151.
6. S. E. Wolf, L. Müller, R. Barrea, C. J. Kampf, J. Leiterer, U. Panne, T. Hoffmann, F. Emmerling and W. Tremel, 2011, **3**, 1158-1165.
7. M. L. Whittaker, P. J. M. Smeets, H. Asayesh-Ardakani, R. Shahbazian-Yassar and D. Joester, *Angew. Chem. Int. Ed.*, 2017, **56**, 16028-16031.
8. S. Leukel, M. Panthöfer, M. Mondeshki, G. Kieslich, Y. Wu, N. Krautwurst and W. Tremel, *J. Am. Chem. Soc.*, 2018, **140**, 14638-14646.

9. M. P. Prange, S. T. Mergelsberg and S. N. Kerisit, *Cryst. Growth Des.*, 2021, **21**, 2212-2221.
10. A. L. Stancik and E. B. Brauns, *Vib. Spectrosc.*, 2008, **47**, 66-69.
11. R. Demichelis, P. Raiteri, J. D. Gale and R. Dovesi, *Cryst. Growth Des.*, 2013, **13**, 2247-2251.
12. S. N. Kerisit and M. P. Prange, *ACS Earth Space Chem.*, 2019, **3**, 2582-2592.
13. M. L. Whittaker and D. Joester, *Adv. Mater.*, 2017, **29**, 1696730.
14. S. T. Mergelsberg, S. L. Riechers, T. R. Graham, M. P. Prange and S. N. Kerisit, *Cryst. Growth Des.*, 2021, **21**, 3384-3393.